



Cite this: *Chem. Commun.*, 2016, 52, 564

Received 17th September 2015,  
Accepted 21st October 2015

DOI: 10.1039/c5cc07793a

www.rsc.org/chemcomm

## Fast lithium-ionic conduction in a new complex hydride–sulphide crystalline phase†

Atsushi Unemoto,<sup>\*a</sup> Hui Wu,<sup>b</sup> Terrence J. Udovic,<sup>b</sup> Motoaki Matsuo,<sup>c</sup>  
Tamio Ikeshoji<sup>ac</sup> and Shin-ichi Orimo<sup>ac</sup>

**A new crystalline phase derived from a 90LiBH<sub>4</sub>:10P<sub>2</sub>S<sub>5</sub> mixture displays high lithium-ionic conductivity of  $\log(\sigma/S \text{ cm}^{-1}) = -3.0$  at 300 K. It is stable up to 473 K and has both a wide potential window of 0–5 V and favorable mechanical properties for battery assembly. Its incorporation into a bulk-type all-solid-state TiS<sub>2</sub>/InLi battery enabled repeated battery operation at 300 K.**

The all-solid-state battery promises a flexible battery design (broader choice of electrodes<sup>1</sup> and bipolar structure<sup>2</sup>) that meets the required energy and power densities and improved safety (by inhibiting lithium dendrite growth, leakage and vaporization of organic liquid electrolytes).<sup>3</sup> Thus, the all-solid-state battery is considered as one of the future-generation energy reservoirs for use in large-scale applications including vehicles, stationary uses for load levelling, and so forth.

Research and development efforts of solid-state electrolytes for all-solid-state batteries have so far been focused mainly on oxides and sulphides.<sup>4–9</sup> Despite extensive explorations of these classes of materials, those that allow for repeated battery operation are limited to a few materials. Thus, interest in looking beyond the traditional electrolytes to other unexplored classes of materials such as complex hydrides<sup>10</sup> to achieve higher-performance batteries is growing. Matsuo *et al.* discovered fast lithium-ionic conduction in the high-temperature phase of LiBH<sub>4</sub> (HT-LiBH<sub>4</sub>) accompanied by an order–disorder transition at around 390 K.<sup>11</sup> Since then, numerous complex hydride-based solid-state fast-ion conductors have been discovered,<sup>12,13</sup> some allowing for repeated all-solid-state battery operation.<sup>14–19</sup>

Despite their advantages for use in all-solid-state batteries, including near unity ion transport numbers, high-temperature durability, a wide potential window, high compatibility with

reactive metallic electrodes and favorable mechanical properties for battery assembly,<sup>13</sup> fast-ion conductors composed solely of complex hydrides discovered thus far exhibit structural-disorder-induced fast-ion conduction at transition temperatures generally higher than room temperature.<sup>12,13,20,21</sup> Realizing fast-ion conduction at reduced temperatures, especially below room temperature, is therefore urgently required.

High reorientational mobility of the complex anion, [BH<sub>4</sub>]<sup>−</sup>, in HT-LiBH<sub>4</sub> allows for inducing ionic carriers and lithium-ion transport channels in the LiBH<sub>4</sub> crystal lattice, and thereby fast lithium-ionic conduction takes place.<sup>22–24</sup> A recent theoretical study revealed that site-to-site hopping is accompanied by rearrangements of the hydrogen coordination number to Li<sup>+</sup> mobile species.<sup>25</sup> Maekawa *et al.* were able to stabilize the HT-LiBH<sub>4</sub> phase down to room temperature by partial replacement of [BH<sub>4</sub>]<sup>−</sup> by iodide ions, I<sup>−</sup>. A larger activation energy,  $E_a$ , of 0.56 eV for Li<sub>4</sub>(BH<sub>4</sub>)<sub>3</sub>I (compared to 0.53 eV for HT-LiBH<sub>4</sub>)<sup>11</sup> reduced the ionic conductivity,  $\sigma$ , at 300 K to  $\log(\sigma/S \text{ cm}^{-1}) = -4.7$ .<sup>26</sup> Thus, a lower  $E_a$  is needed to maintain fast-ion conduction at reduced temperatures. More recently, Yamauchi *et al.* formed a fast lithium-ionic conductor by dispersing a small concentration of LiBH<sub>4</sub> into a 75Li<sub>2</sub>S–25P<sub>2</sub>S<sub>5</sub> glass matrix. It possesses the high lithium-ionic conductivity of  $\log(\sigma/S \text{ cm}^{-1}) = -2.8$  at 298 K with a reduced  $E_a$  of 0.22 eV. The high conductivity and reduced  $E_a$  were attributed to a delocalized charge on the reorienting [BH<sub>4</sub>]<sup>−</sup>-unit within the glass matrix, weakening the electrostatic interaction between Li<sup>+</sup> and [BH<sub>4</sub>]<sup>−</sup>.<sup>27</sup> These studies indicate that a search for other hybrid complex-hydride/sulphide materials would be beneficial for finding additional promising Li<sup>+</sup> conductors with low activation energies.

Here we report on a pseudo-binary system composed of a complex hydride and sulphide, namely  $x\text{LiBH}_4-(100-x)\text{P}_2\text{S}_5$  ( $0 \leq x \leq 100$ ). Within this system, a new crystalline phase appeared for  $x = 90$  (hereafter denoted by “90LiBH<sub>4</sub>:10P<sub>2</sub>S<sub>5</sub>”). It possessed high lithium-ionic conductivity of  $\log(\sigma/S \text{ cm}^{-1}) = -3.0$  at 300 K, a low activation energy of 0.38 eV without phase transition within a wide temperature range of 4–473 K, a wide potential window of 0–5 V, and favourable mechanical

<sup>a</sup> WPI-Advanced Institute for Materials Research (WPI-AIMR), Tohoku University, Sendai 980-8577, Japan. E-mail: unemoto@imr.tohoku.ac.jp

<sup>b</sup> NIST Center for Neutron Research, National Institute of Standards and Technology, Gaithersburg, MD 20899-6102, USA

<sup>c</sup> Institute for Materials Research, Tohoku University, Sendai 980-8577, Japan

† Electronic supplementary information (ESI) available: Experimental procedures and additional experimental results. See DOI: 10.1039/c5cc07793a

properties for battery assembly. These allowed for repeated discharge–charge cycles of a bulk-type all-solid-state  $\text{TiS}_2/\text{InLi}$  battery at 300 K.

The powder X-ray diffraction (XRD) patterns of the pseudo-binary system,  $x\text{LiBH}_4-(100-x)\text{P}_2\text{S}_5$ , indicate that a new crystalline phase precipitated with the highest concentration when  $x = 90$ ,  $90\text{LiBH}_4:10\text{P}_2\text{S}_5$  (see powder X-ray and neutron powder diffraction patterns in the ESI,† Fig. S1). Although by no means certain, the XRD patterns could be indexed to a possible orthorhombic structure. The relative losses of B and H throughout the synthesis (with approximately 30% and 45%, respectively, and  $\text{H/B} \sim 3.2$ ) evaluated by means of neutron prompt gamma-ray activation analysis (PGAA) and neutron vibrational (NV) spectra of  $90^7\text{Li}^{11}\text{BH}_4:10\text{P}_2\text{S}_5$  suggest that some or all of the original  $[\text{BH}_4]^-$  ions may be transformed to  $-\text{BH}_3$ ,  $=\text{BH}_2$ , and/or  $\equiv\text{BH}$  fragments as part of a larger unknown complex anion (see NV spectra and elastic incoherent structure factor dependence on momentum transfer in the ESI,† Fig. S2 and S3, respectively). Differential scanning calorimetry (DSC) suggests that the new phase is stable upon cycling from room temperature to 473 K (see the DSC profile in the ESI,† Fig. S4).

The pseudo-binary  $x\text{LiBH}_4-(100-x)\text{P}_2\text{S}_5$  had the greatest conductivity regardless of the temperature, and the lowest  $E_a$  for  $x = 90$ , *i.e.*,  $90\text{LiBH}_4:10\text{P}_2\text{S}_5$  (also see the conductivities of  $x\text{LiBH}_4-(100-x)\text{P}_2\text{S}_5$  in the ESI,† Fig. S5). DC measurements with symmetric cell configurations identified that the major carriers in  $90\text{LiBH}_4:10\text{P}_2\text{S}_5$  were the lithium-ions (see ESI,† Fig. S6). The lithium-ionic conductivity of  $90\text{LiBH}_4:10\text{P}_2\text{S}_5$  at 300 K was as high as  $\log\{\sigma(300\text{ K})\} = -3.0$ , and  $E_a$  was 0.38 eV (compared to 0.53 eV for  $\text{HT-LiBH}_4$ ), as shown in Fig. 1.<sup>11</sup> The ionic conductivity and activation energy are comparable to  $\text{Li}_{0.34}\text{La}_{0.51}\text{TiO}_{2.94}$ .<sup>8</sup> Contrary to pure  $\text{LiBH}_4$ ,<sup>11</sup> a conductivity jump accompanied by a structural transition was not observed within the studied temperature range (see also the DSC profiles in the ESI,† Fig. S4). Although we explored the pseudo-ternary system,  $\text{LiBH}_4\text{-P}_2\text{S}_5\text{-Li}_2\text{S}$ , no other new crystalline phase appeared by means of our synthetic route employed here (see conductivities in the ESI,† Fig. S7).

Owing to the complexity of the  $90\text{LiBH}_4:10\text{P}_2\text{S}_5$  crystal chemistry, further investigations are required to solve its structure.

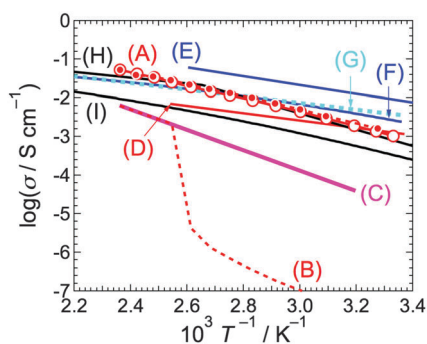


**Fig. 1** Lithium-ionic conductivities of (A)  $90\text{LiBH}_4:10\text{P}_2\text{S}_5$ , where closed and open symbols show the values obtained during heating and cooling runs, respectively. The conductivity is compared to those of other materials: (B)  $\text{LiBH}_4$ ,<sup>11</sup> (C)  $\text{Li}_4(\text{BH}_4)_3$ ,<sup>26</sup> (D)  $33\text{LiBH}_4-67(\text{Li}_2\text{S}-\text{P}_2\text{S}_5)$  glass,<sup>27</sup> (E)  $\text{Li}_{10}\text{GeP}_2\text{S}_{12}$ ,<sup>5</sup> (F)  $\text{Li}_7\text{P}_3\text{S}_{11}$  glass-ceramics,<sup>6</sup> (G)  $\text{Li}_{0.325}\text{Ge}_{0.25}\text{P}_{0.75}\text{S}_4$  (thio-LISICON),<sup>7</sup> (H)  $\text{Li}_{0.34}\text{La}_{0.51}\text{TiO}_{2.94}$ ,<sup>8</sup> and (I)  $\text{Li}_7\text{La}_3\text{Zr}_2\text{O}_{12.9}$ .

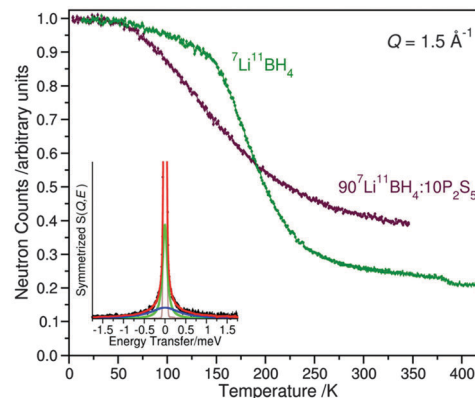


**Fig. 2** Neutron FWs at  $+0.25\text{ K min}^{-1}$ ,  $0.8\text{ }\mu\text{eV}$  fwhm resolution, and  $1.5\text{ }\text{\AA}^{-1}$  neutron momentum transfer for  $90^7\text{Li}^{11}\text{BH}_4:10\text{P}_2\text{S}_5$  and  $^7\text{Li}^{11}\text{BH}_4$ . Inset: Corresponding 300 K QENS spectrum for  $90^7\text{Li}^{11}\text{BH}_4:10\text{P}_2\text{S}_5$ , fit with a resolution function (brown) and two Lorentzian components (green + blue).

On the other hand, fast-ion conduction in complex hydrides is known to be associated with a high reorientational mobility for the resident anions, as seen for the high-temperature phases of  $\text{LiBH}_4$ ,<sup>22-25</sup>  $\text{Na}_2\text{B}_{12}\text{H}_{12}$ ,<sup>20</sup> and  $\text{Na}_2\text{B}_{10}\text{H}_{10}$ .<sup>21</sup> We thus decided to investigate the dynamics of the hydrogen-containing anionic units in  $90^7\text{Li}^{11}\text{BH}_4:10\text{P}_2\text{S}_5$  by means of quasielastic neutron scattering (QENS). Elastic-scattering fixed-window scans (FWs)<sup>28</sup> for  $90^7\text{Li}^{11}\text{BH}_4:10\text{P}_2\text{S}_5$  and  $^7\text{Li}^{11}\text{BH}_4$  are shown in Fig. 2. A comparison of the relative decreases in intensity with temperature suggests that about one-fourth to one-third of the H atoms in  $90\text{LiBH}_4:10\text{P}_2\text{S}_5$  are “reorientationally immobile” ( $<10^8\text{ H jumps s}^{-1}$ ) on the neutron timescale up to at least 350 K. Different scenarios could explain this, *e.g.*, the presence of a mixture of (mobile)  $[\text{BH}_4]^-$  anions and (immobile)  $=\text{BH}_2$  fragments. The momentum-transfer dependences of the quasielastic fraction (see ESI,† Fig. S3) and widths are consistent with this observation and suggest localized  $2\text{ }\text{\AA}$  H jumps, in agreement with the H–H distances in both  $[\text{BH}_4]^-$  and  $-\text{BH}_3$ . The QENS spectrum at 300 K in Fig. 2 hints that there are two different quasielastic components of comparable intensities from two hydrogenous entities. The different widths (and thus reorientational mobilities) correspond to relative jump frequencies of the order of  $10^{11}$  and  $6 \times 10^{11}\text{ s}^{-1}$ . Although these values are reminiscent of what is observed for the relative  $[\text{BH}_4]^-$  mobilities in orthorhombic and  $\text{HT-LiBH}_4$ ,<sup>29</sup> we will not know the true nature of these mobile species until we are able to determine the corresponding crystal structure. Nonetheless, we may reasonably speculate that these high anion-related mobilities are a factor in promoting the fast-ion conductivity.<sup>20-25</sup>

Our new  $90\text{LiBH}_4:10\text{P}_2\text{S}_5$  electrolyte had a wide potential window of 0–5 V at 300 K. In a cyclic voltammogram, reversible lithium dissolution/stripping took place at nearly 0 V and no irreversible oxidation current was observed up to 5 V on the stainless-steel (SUS) electrode (see the CV profile in the ESI,† Fig. S8). Thus, this new material has sufficient electrochemical stability to be incorporated into an all-solid-state battery.

The high deformability of the constituent materials is also one of the important requirements for a “bulk-type” all-solid-state battery assembly,<sup>30</sup> which contains a high quantity of electrode-active materials in the electrode layer. Our  $90\text{LiBH}_4:10\text{P}_2\text{S}_5$  consists

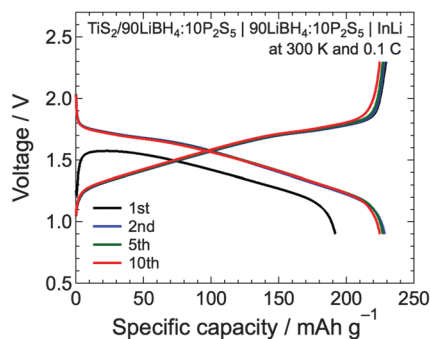


Fig. 3 Discharge-charge profiles of the bulk-type all-solid-state  $\text{TiS}_2/\text{InLi}$  battery using the  $90\text{LiBH}_4:10\text{P}_2\text{S}_5$  electrolyte operated at 300 K and 0.1 C ( $114 \mu\text{A cm}^{-2}$ ).

of the highly deformable complex hydride<sup>13,17,18</sup> and sulphide.<sup>30</sup> It enables the preparation of a compacted electrolyte and its intimate contact with the  $\text{TiS}_2$  active material in the composite positive electrode layer merely by cold-pressing (see the microstructure image of the composite positive electrode layer in the ESI,† Fig. S9). Such a robust interface facilitates smooth charge transfer between layers during battery operation.<sup>13,17–19,30</sup>

As we expected, repeated operation of the bulk-type all-solid-state  $\text{TiS}_2/\text{InLi}$  battery with the  $90\text{LiBH}_4:10\text{P}_2\text{S}_5$  electrolyte was successfully realized at 300 K and 0.1 C ( $114 \mu\text{A cm}^{-2}$ ), as shown in Fig. 3 (the electrolyte thickness was 500  $\mu\text{m}$ ).  $\text{TiS}_2$  has a theoretical capacity of 239  $\text{mA h g}^{-1}$ .<sup>31</sup> Our battery exhibited initial and second discharge capacities of 192 and 228  $\text{mA h g}^{-1}$ , respectively. Reversible specific capacities with nearly 100% coulombic efficiency were realized after the initial cycle (also see the battery test result with a different battery configuration, Fig. S11, ESI†). As a result, the 10th discharge capacity retention ratio (to the 2nd discharge) remained as high as 98%. We are currently evaluating, in more detail, the cycle stability as well as the power density of bulk-type all-solid-state batteries using this new  $90\text{LiBH}_4:10\text{P}_2\text{S}_5$  electrolyte.

In conclusion, a new crystalline, fast lithium-ionic conductor,  $90\text{LiBH}_4:10\text{P}_2\text{S}_5$ , composed of complex hydride and sulphide components was discovered in this study. Its fast lithium-ionic conduction may be assisted by the high reorientational mobility associated with the anions, similar to other complex hydride-based, solid-state, fast ionic conductors.<sup>11,20,21</sup> Unlike electrolytes composed solely of complex hydrides,<sup>11,20,21</sup> no phase transition was observed in the wide temperature range of 4–473 K, and thereby a high lithium ionic conductivity,  $\log(\sigma/\text{S cm}^{-1}) = -3.0$ , at 300 K was realized. The new phase also possesses a wide potential window of 0–5 V and high temperature durability up to 473 K. Highly deformable  $90\text{LiBH}_4:10\text{P}_2\text{S}_5$  allowed for assembling a bulk-type all-solid-state  $\text{TiS}_2/\text{InLi}$  battery merely by cold-pressing. Repeated operation of this battery was demonstrated at 300 K. The results obtained in this study provide principles for exploring new electrolytes for high-performance, all-solid-state, energy-storage devices.

The authors would like to thank Mr K. Sato, Ms H. Ohmiya, Ms N. Warifune, and Dr R. L. Paul for technical assistance. The fruitful discussion and collaboration with Mr G. Nogami and Dr M. Taniguchi of Mitsubishi Gas Chemicals Co., Ltd are

also acknowledged. This study was performed in part as collaboration between members of IEA HIA Task 32, Hydrogen-based Energy Storage. The authors gratefully acknowledge support from DOE EERE through Grant No. DE-EE0002978; the Target Project 4 of WPI-AIMR, Tohoku University; Collaborative Research Centre on Energy Materials, Tohoku University; JSPS KAKENHI Grant No. 25220911; and the Advanced Low Carbon Technology Research and Development Program (ALCA) from the Japan Science and Technology Agency (JST).

## Notes and references

- P. G. Bruce, S. A. Freunberger, L. J. Hardwick and J.-M. Tarascon, *Nat. Mater.*, 2012, **11**, 19.
- Y. Kato, K. Kawamoto, R. Kanno and M. Hirayama, *Electrochemistry*, 2012, **80**, 749.
- K. Takada, *Acta Mater.*, 2013, **61**, 759.
- J. W. Fergus, *J. Power Sources*, 2010, **195**, 4554.
- N. Kamaya, K. Homma, Y. Yamakawa, M. Hirayama, R. Kanno, M. Yonemura, T. Kamiyama, Y. Kato, S. Hama, K. Kawamoto and A. Mitsui, *Nat. Mater.*, 2011, **10**, 682.
- F. Mizuno, A. Hayashi, K. Tadanaga and M. Tatsumisago, *Adv. Mater.*, 2005, **17**, 918.
- R. Kanno and M. Murayama, *J. Electrochem. Soc.*, 2001, **148**, A742.
- Y. Inaguma, C. Liqun, M. Itoh and T. Nakamura, *Solid State Commun.*, 1993, **86**, 689.
- R. Murugan, V. Thangadurai and W. Weppner, *Angew. Chem., Int. Ed.*, 2007, **46**, 7778.
- S. Orimo, Y. Nakamori, J. R. Eliseo, A. Züttel and C. M. Jensen, *Chem. Rev.*, 2007, **107**, 4111.
- M. Matsuo, Y. Nakamori, S. Orimo, H. Maekawa and H. Takamura, *Appl. Phys. Lett.*, 2007, **91**, 224103.
- M. Matsuo and S. Orimo, *Adv. Energy Mater.*, 2011, **1**, 161.
- A. Unemoto, M. Matsuo and S. Orimo, *Adv. Funct. Mater.*, 2014, **24**, 2267.
- K. Takahashi, K. Hattori, T. Yamazaki, K. Takada, M. Matsuo, S. Orimo, H. Maekawa and H. Takamura, *J. Power Sources*, 2013, **226**, 61.
- K. Takahashi, H. Maekawa and H. Takamura, *Solid State Ionics*, 2014, **262**, 179.
- D. Sveinbjörnsson, A. S. Christiansen, R. Viskinde, P. Norby and T. Vegge, *J. Electrochem. Soc.*, 2014, **161**, A1432.
- A. Unemoto, S. Yasaku, G. Nogami, M. Tazawa, M. Taniguchi, M. Matsuo, T. Ikeshoji and S. Orimo, *Appl. Phys. Lett.*, 2014, **105**, 083901.
- A. Unemoto, C. Chen, Z. Wang, M. Matsuo, T. Ikeshoji and S. Orimo, *Nanotechnology*, 2015, **26**, 254001.
- A. Unemoto, T. Ikeshoji, S. Yasaku, M. Matsuo, V. Stavila, T. J. Udovic and S. Orimo, *Chem. Mater.*, 2015, **27**, 5407.
- T. J. Udovic, M. Matsuo, A. Unemoto, N. Verdál, V. Stavila, A. V. Skripov, J. J. Rush, H. Takamura and S. Orimo, *Chem. Commun.*, 2014, **50**, 3750.
- T. J. Udovic, M. Matsuo, W. S. Tang, H. Wu, V. Stavila, A. V. Soloninin, R. V. Skoryunov, O. A. Babanova, A. V. Skripov, J. J. Rush, A. Unemoto, H. Takamura and S. Orimo, *Adv. Mater.*, 2014, **26**, 7622.
- T. Ikeshoji, E. Tsuchida, K. Ikeda, M. Matsuo, H.-W. Li, Y. Kawazoe and S. Orimo, *Appl. Phys. Lett.*, 2009, **95**, 221901.
- T. Ikeshoji, E. Tsuchida, T. Morishita, K. Ikeda, M. Matsuo, Y. Kawazoe and S. Orimo, *Phys. Rev. B: Condens. Matter Mater. Phys.*, 2011, **83**, 144301.
- J. S. G. Myrdal, D. Blanchard, D. Sveinbjörnsson and T. Vegge, *J. Phys. Chem. C*, 2013, **117**, 9084.
- T. Ikeshoji, Y. Ando, M. Otani, E. Tsuchida, S. Takagi, M. Matsuo and S. Orimo, *Appl. Phys. Lett.*, 2013, **103**, 133903.
- H. Maekawa, M. Matsuo, H. Takamura, M. Ando, Y. Noda, T. Karahashi and S. Orimo, *J. Am. Chem. Soc.*, 2009, **131**, 894.
- A. Yamauchi, A. Sakuda, A. Hayashi and M. Tatsumisago, *J. Power Sources*, 2013, **244**, 707.
- T. J. Udovic, N. Verdál, J. J. Rush, D. J. De Vries, M. R. Hartman, J. J. Vajo, A. F. Gross and A. V. Skripov, *J. Alloys Compd.*, 2013, **580**, S47.
- N. Verdál, T. J. Udovic, J. J. Rush, X. Liu, E. H. Majzoub, J. J. Vajo and A. F. Gross, *J. Phys. Chem. C*, 2013, **117**, 17983.
- A. Sakuda, A. Hayashi and M. Tatsumisago, *Sci. Rep.*, 2013, **3**, 2261.
- M. S. Whittingham, *Science*, 1976, **192**, 1126; M. S. Whittingham, *Prog. Solid State Chem.*, 1978, **12**, 41.

Electronic Supporting Information (ESI) for:

## Fast lithium-ionic conduction in a new complex hydride–sulphide crystalline phase

Atsushi Unemoto,<sup>a,\*</sup> Hui Wu,<sup>b</sup> Terrence J. Udovic,<sup>b</sup> Motoaki Matsuo,<sup>c</sup> Tamio Ikeshoji,<sup>a,c</sup> and Shin-ichi Orimo<sup>a,c</sup>

<sup>a</sup>WPI–Advanced Institute for Materials Research, Tohoku University, Sendai 980-8577, Japan.

<sup>b</sup>NIST Center for Neutron Research, National Institute of Standards and Technology, Gaithersburg, MD 20899-6102, USA

<sup>c</sup>Institute for Materials Research, Tohoku University, Sendai 980-8577, Japan.

\*E-mail: unemoto@imr.tohoku.ac.jp

The mention of all commercial suppliers in this paper is for clarity. This does not imply the recommendation or endorsement of these suppliers by NIST.

### *Preparation of complex hydride–sulfide crystals*

A pseudo-ternary system,  $\text{LiBH}_4\text{--P}_2\text{S}_5\text{--Li}_2\text{S}$ , was divided into four pseudo-binary systems, namely  $x\text{LiBH}_4\text{--}(100\text{--}x)\text{P}_2\text{S}_5$  ( $x = 97.5, 95, 90, 87.5, 85, 80$  and  $67$ ),  $y\text{LiBH}_4\text{--}(100\text{--}y)\text{Li}_2\text{S}$  ( $y = 90, 75$  and  $50$ ),  $p(90\text{LiBH}_4\text{--}10\text{P}_2\text{S}_5)\text{--}(100\text{--}p)\text{Li}_2\text{S}$  ( $p = 90, 75, 65, 50$  and  $25$ ) and  $q(90\text{LiBH}_4\text{--}10\text{P}_2\text{S}_5)\text{--}(100\text{--}q)(90\text{LiBH}_4\text{--}10\text{Li}_2\text{S})$  ( $q = 75, 50$  and  $25$ ). The powders of  $\text{LiBH}_4$  ( $> 95\%$ , Sigma-Aldrich),  $\text{P}_2\text{S}_5$  ( $99\%$ , Sigma-Aldrich) and  $\text{Li}_2\text{S}$  ( $99.98\%$ , Sigma-Aldrich) were used as starting materials. These powders were weighed in desired ratios, and mixed in an agate mortar with an agate pestle, and further mixed via planetary ball-milling (Fritsch, P-7) at a rotation rate of 400 rpm for 5 h with 20 stainless-steel balls having 8-mm-diameter. The resultant powders were annealed at 423 K for 2 h in an Ar-filled environment.

### *Discussion on crystal structures*

The X-ray diffraction (XRD) measurements were carried out for the product powders. The resultant powder after the mechanical ball milling and subsequent annealing was placed into a glass capillary with 0.5 mm inner diameter. The XRD patterns were collected with  $\text{CuK}\alpha$  radiation (X'pert PRO, PANalytical).

Powder XRD patterns of the pseudo-binary system comprising of  $\text{LiBH}_4$  and  $\text{P}_2\text{S}_5$  obtained at room temperature are shown in Fig. S1 (a). Those of the as-received  $\text{LiBH}_4$  and  $\text{P}_2\text{S}_5$  are also shown for comparison. Within this pseudo-binary system, only broadened patterns were obtained for  $x \leq 80$  in  $x\text{LiBH}_4\text{--}(100\text{--}x)\text{P}_2\text{S}_5$ . Diffraction peaks from a new crystalline phase appeared with increasing  $x$ . When  $x$  exceeds 95, diffraction peaks owing to unreacted/remaining  $\text{LiBH}_4$  appeared. The results suggest that the new crystalline phase precipitates in the highest concentration for  $85 \leq x \leq 95$ . The XRD patterns appearing for  $90\text{LiBH}_4\text{:}10\text{P}_2\text{S}_5$  could be indexed by an orthorhombic system with lattice parameters of  $a = 5.061 \text{ \AA}$ ,  $b = 7.149 \text{ \AA}$  and  $c = 11.805 \text{ \AA}$ .

Additional neutron powder diffraction (NPD) measurements using the NIST BT-1 High-Resolution Neutron Powder Diffractometer were carried out at 4 K and 295 K for  $90\text{Li}^{11}\text{BD}_4\text{:}10\text{P}_2\text{S}_5$ . Here,  $\text{Li}^{11}\text{BD}_4$  (Katchem) was used instead of  $\text{LiBH}_4$  in the starting materials. The sample was prepared in the same manner as described above.

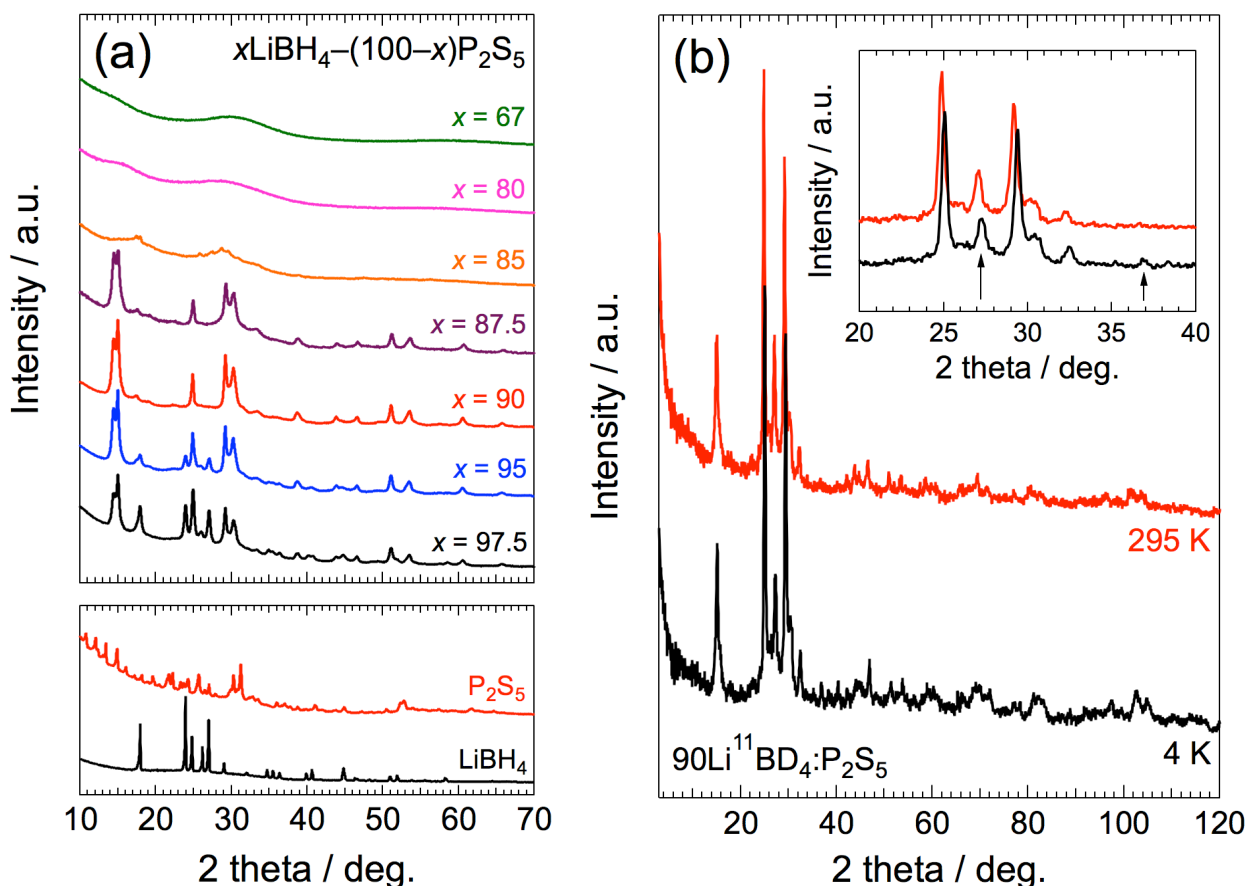


**FIGURE S1.** (a) Powder XRD patterns of a pseudo-binary system,  $x\text{LiBH}_4-(100-x)\text{P}_2\text{S}_5$  ( $x = 97.5, 95, 90, 87.5, 85, 80$  and  $67$ ), obtained at room temperature as a function of  $x$ . The as-received  $\text{P}_2\text{S}_5$  and  $\text{LiBH}_4$  were also shown for comparison. (b) NPD patterns of  $90\text{Li}^{11}\text{BD}_4:10\text{P}_2\text{S}_5$  obtained at 4 K (black) and 295 K (red). Inset: NPD patterns of  $90\text{Li}^{11}\text{BD}_4:10\text{P}_2\text{S}_5$  in narrower diffraction angle. The arrows represent the diffraction peaks of  $\text{Li}^{11}\text{BD}_4$ .

### Prompt gamma activation analysis

Since the actual elemental ratios (i.e., chemical formula) of the new crystalline phase in  $90\text{LiBH}_4:10\text{P}_2\text{S}_5$  are unknown and may be different from those of the starting materials, we decided to estimate the constituent element ratios of the post-ball-milled/annealed materials. Neutron prompt gamma-ray activation analysis (PGAA; a quantitative analysis technique) using the NIST NGD cold-neutron PGAA spectrometer [S1], was employed to determine the elemental ratios in treated  $90\text{LiBH}_4:10\text{P}_2\text{S}_5$ . Here, an additional  $90^7\text{Li}^{11}\text{BH}_4:10\text{P}_2\text{S}_5$  sample was prepared using  $^7\text{Li}^{11}\text{BH}_4$  (Katchem) in the starting materials. From PGAA of both samples and  $^7\text{Li}^{11}\text{BH}_4$ ,  $\text{LiBH}_4$ ,  $\text{Li}_2\text{SO}_4$ ,  $\text{Li}_3\text{PO}_4$  and  $\text{Li}_2\text{SO}_4/\text{Li}_3\text{PO}_4$  mixtures, we were able to obtain estimates of these elemental ratios. Although  $90\text{LiBH}_4:10\text{P}_2\text{S}_5$  nominally contains  $\text{Li}:\text{B}:\text{H}:\text{P}:\text{S} = 90:90:360:20:50$ , the PGAA-derived ratios were  $90:63:204:18:46$  ( $\text{S}/\text{P} = 2.55(5)$ ,  $\text{H}/\text{B} = 3.219(3)$ ,  $\text{Li}/\text{S} = 1.96(2)$  and  $\text{Li}/\text{B} = 1.42(2)$ ). This suggests that B and H were reduced during the synthesis as gaseous species and/or precipitates, and as a result, some or all of the original  $[\text{BH}_4]^-$  anions in  $90\text{LiBH}_4:10\text{P}_2\text{S}_5$  no longer remain intact.

## Neutron vibrational spectrometry

To examine what hydrogenous species are present in  $90\text{LiBH}_4:10\text{P}_2\text{S}_5$ , we performed neutron vibrational spectroscopy (NVS) measurements of both  $90^7\text{Li}^{11}\text{BH}_4:10\text{P}_2\text{S}_5$  and  $90\text{Li}^{11}\text{BD}_4:10\text{P}_2\text{S}_5$  using the NIST Filter-Analyzer Neutron Spectrometer [S2]. Due to the overwhelmingly high incoherent neutron scattering cross section for H relative to other elements, NV spectra are dominated by vibrational modes involving H displacements. A comparison of these 4 K NV spectra with those for  $\text{LiBH}_4$ ,  $\text{Li}_2\text{BH}_4\text{I}$  [S3],  $\text{NH}_3\text{BH}_3$  [S4],  $\text{N}_2\text{H}_4\text{BH}_3$  [S5], and  $\text{LiH}$  are shown in Fig. S2. The  $90\text{Li}^{11}\text{BD}_4:10\text{P}_2\text{S}_5$  spectrum is a slightly anharmonic energy-downscaled (energy $\times 0.76$ ) version of the  $90^7\text{Li}^{11}\text{BH}_4:10\text{P}_2\text{S}_5$  spectrum due to the doubled mass of D atoms compared to H atoms. It is clear that the  $90^7\text{Li}^{11}\text{BH}_4:10\text{P}_2\text{S}_5$  spectrum does not resemble that for orthorhombic (o)  $\text{LiBH}_4$ , although there are similarities in the B–H bending mode region between 130 meV and 170 meV. The  $90^7\text{Li}^{11}\text{BH}_4:10\text{P}_2\text{S}_5$  spectrum does not have the well-defined  $[\text{BH}_4]^-$  translational and librational bands of o- $\text{LiBH}_4$  near 27 meV and 52 meV (but rather only more broadened features somewhat like for  $\text{Li}_2\text{BH}_4\text{I}$ , which is a hexagonal (h) disordered solid-solution of  $\text{LiBH}_4$  and  $\text{LiI}$ ), and there is an additional B–H bending mode band for the former near 150 meV that is absent for o- $\text{LiBH}_4$ . Moreover, the  $90^7\text{Li}^{11}\text{BH}_4:10\text{P}_2\text{S}_5$  spectrum possesses an additional non- $[\text{BH}_4]^-$ -like fundamental band near 100 meV that is also absent for both o- $\text{LiBH}_4$  and h- $\text{Li}_2\text{BH}_4\text{I}$ . (N.B., the minor o- $\text{LiBH}_4$  bands near 75 and 100 meV are combination and overtone bands due to the sharp fundamental modes at lower energy.) The extra  $90^7\text{Li}^{11}\text{BH}_4:10\text{P}_2\text{S}_5$  features near 100 meV and 150 meV are more reminiscent of rocking and bending modes, respectively, of a  $-\text{BH}_3$  fragment, as observed for  $\text{NH}_3\text{BH}_3$  [S4] and  $\text{N}_2\text{H}_4\text{BH}_3$  [S5]. Yet, other  $\text{BH}_x$  fragments or even fragments involving P–H or S–H bonds cannot be discounted at this point. In fact,  $\text{LiH}$  also displays a band near 95 meV, although its higher accompanying 128 meV band is not present in the  $90^7\text{Li}^{11}\text{BH}_4:10\text{P}_2\text{S}_5$  spectrum.

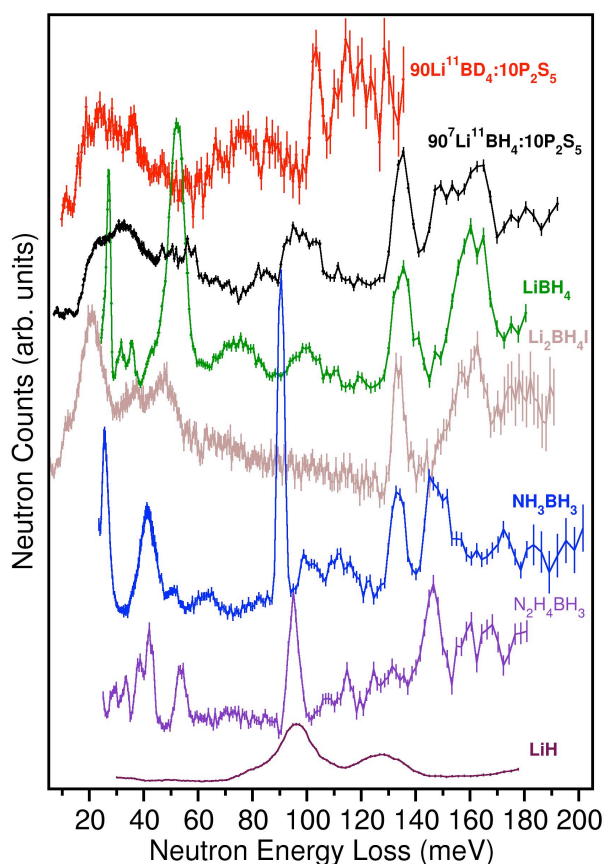


**FIGURE S2.** Neutron vibrational spectra of  $90\text{Li}^{11}\text{BD}_4:10\text{P}_2\text{S}_5$ ,  $90^7\text{Li}^{11}\text{BH}_4:10\text{P}_2\text{S}_5$ ,  $\text{LiBH}_4$ ,  $\text{Li}_2\text{BH}_4\text{I}$  solid solution [S3],  $\text{NH}_3\text{BH}_3$  [S4],  $\text{N}_2\text{H}_4\text{BH}_3$  [S5], and  $\text{LiH}$  obtained at 4 K.

## Quasi-elastic neutron scattering

Quasielastic neutron scattering measurements on  $90^7\text{Li}^{11}\text{BH}_4:10\text{P}_2\text{S}_5$  and  $^7\text{Li}^{11}\text{BH}_4$  were carried out using the NIST High-Flux Backscattering Spectrometer [S6] for the fixed-window scans (FWSs) shown in Fig. 2 of the paper, and the NIST Disk Chopper Spectrometer (DCS) [S7] for complementary quasielastic spectra (as exemplified in the Fig. 2 inset). The QENS data were treated with the DAVE software package [S8]. The comparison of the FWSs for  $90^7\text{Li}^{11}\text{BH}_4$  in Fig. 2 indicate an earlier onset for H mobility for  $90^7\text{Li}^{11}\text{BH}_4:10\text{P}_2\text{S}_5$  (at  $\sim 80$  K) compared to that for  $^7\text{Li}^{11}\text{BH}_4$  (at  $\sim 160$  K). Also, the decreasing FWS slope is more gradual for  $90^7\text{Li}^{11}\text{BH}_4:10\text{P}_2\text{S}_5$ , suggesting a smaller activation energy for H jump reorientations than for  $^7\text{Li}^{11}\text{BH}_4$  and/or a distribution of H mobilities.

We found that the DCS QENS spectra for  $90^7\text{Li}^{11}\text{BH}_4:10\text{P}_2\text{S}_5$ , were better fit with two different Lorentzian components along with the expected additional delta function, all convoluted with the instrumental resolution function measured below 50 K. Figure S3 illustrates the resulting elastic incoherent structure factor (EISF) dependence on momentum transfer  $Q$  for  $90^7\text{Li}^{11}\text{BH}_4:10\text{P}_2\text{S}_5$  at both 300 and 325 K assuming two Lorentzian components (with Lorentzian fwhm widths of 0.13 and 0.84 meV at 300 K and 0.20 and 1.67 meV at 325 K). The shape and position of the EISF minimum suggests a single H-H jump distance of  $\sim 2$  Å, consistent with the H-H distances associated with both  $[\text{BH}_4]^-$  anions and  $-\text{BH}_3$  fragments. The data fit within an EISF band that is consistent with one-fourth to one-third of the H atoms in the material remaining immobile (such as in  $=\text{BH}_2$ ,  $\equiv\text{BH}_3$ ,  $-\text{SH}$ ,  $-\text{PH}$ , or LiH species) while the rest undergo 3-fold (such as for  $-\text{BH}_3$ ) and/or tetrahedral tumbling motions (such as for  $[\text{BH}_4]^-$  anions). We will have a much clearer picture of the H dynamics after the unknown crystal structure is finally determined.

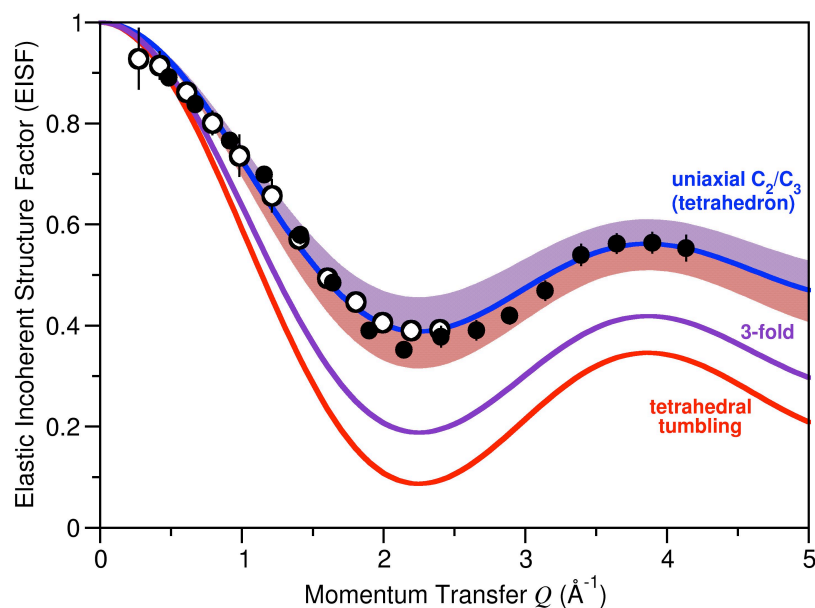


**FIGURE S3.** Elastic incoherent structure factor (EISF) vs. momentum transfer  $Q$  for  $90^7\text{Li}^{11}\text{BH}_4:10\text{P}_2\text{S}_5$  assumed two Lorentzian components: at 300 K for 4.8 Å neutrons (56  $\mu\text{eV}$  fwhm resolution; open circles) and at 325 K for 2.75 Å neutrons (275  $\mu\text{eV}$  fwhm resolution; closed circles). Red, purple, and blue curves denote three respective H jump models, assuming a H-H jump distance of 2 Å: tumbling of H among four-corners of a tetrahedron (such as for  $[\text{BH}_4]^-$ ), 3-fold uniaxial reorientation (such as for  $-\text{BH}_3$ ), and uniaxial  $C_2$  or  $C_3$  reorientations of H in a tetrahedral configuration (such as for  $[\text{BH}_4]^-$ ). (N.B., the latter model is indistinguishable to that for 3-fold  $-\text{BH}_3$  jumps with an additional immobile H atom present). The mauve and pink bands encompass the swath of EISF models where one-fourth to one-third of the H atoms present in the material remain immobile while the rest undergo 3-fold (mauve EISF band) and/or tetrahedral tumbling motions (pink EISF band).

### Differential scanning calorimetry

Differential scanning calorimetry (DSC) was carried out for the as-ball milled  $90\text{LiBH}_4 + 10\text{P}_2\text{S}_5$  (without heating) and the as-synthesized powders at a heating rate of  $5\text{ K min}^{-1}$  for two temperature cycles. A reference  $\text{Al}_2\text{O}_3$  powder and an Al pan were used for the measurements. During measurements, the temperature was kept at 473 K for 1 h after the samples reached this temperature. During the initial heating run of the as-ball-milled  $90\text{LiBH}_4 + 10\text{P}_2\text{S}_5$ , distinct endothermic peaks appeared at 332, 379 and 428 K while exothermic peaks appeared at 341 and 389 K, as shown in Fig. S4 (a). No peaks were observed during the 1<sup>st</sup> cooling and subsequent 2<sup>nd</sup> heating and cooling runs. The DSC profiles of the as-synthesized  $90\text{LiBH}_4:10\text{P}_2\text{S}_5$  do not have any remarkable peaks during the temperature scan, as shown in Fig. S4 (b). The results suggest that the peaks appearing for the mixed  $\text{LiBH}_4$  and  $\text{P}_2\text{S}_5$  powder arise mainly from the formation process of a new crystalline phase in  $90\text{LiBH}_4:10\text{P}_2\text{S}_5$ . The annealing at 423 K for 2 h in an Ar atmosphere, which we also employed for the synthesis, is sufficient to complete the formation reaction of  $90\text{LiBH}_4:10\text{P}_2\text{S}_5$ .  $90\text{LiBH}_4:10\text{P}_2\text{S}_5$  does not undergo a phase transition within the temperature range of the DSC measurement, contrary to  $\text{LiBH}_4$  [S9]. This means that unreacted/remaining  $\text{LiBH}_4$  in  $90\text{LiBH}_4:10\text{P}_2\text{S}_5$  is negligibly small, and is consistent with the result of the conductivity measurement that a visible conductivity jump did not occur over the temperature range investigated, as shown in Figs. 1 and S5.

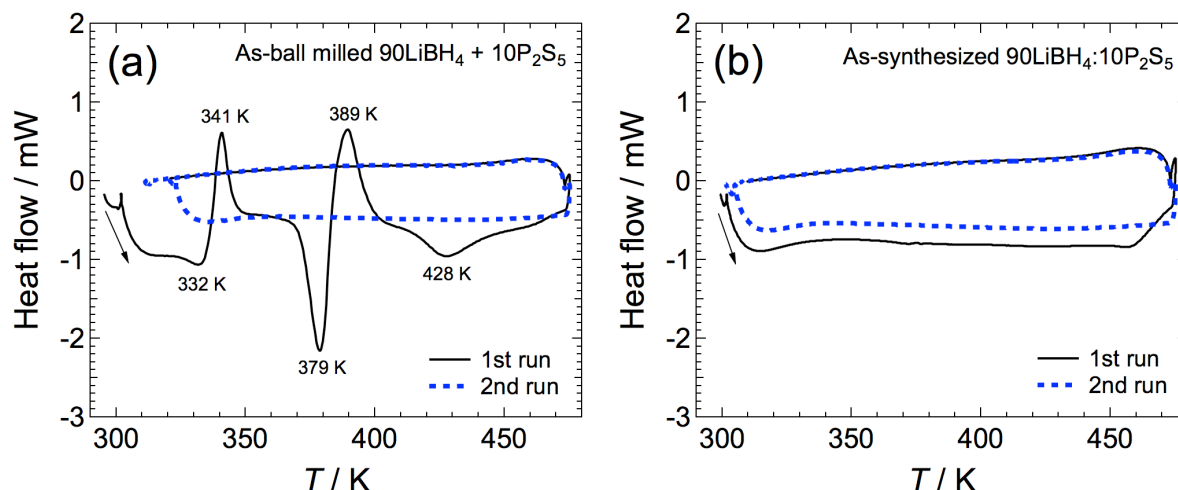


**FIGURE S4.** DSC profiles of (a) the as-milled  $90\text{LiBH}_4 + 10\text{P}_2\text{S}_5$  and (b) the as-synthesized  $90\text{LiBH}_4:10\text{P}_2\text{S}_5$  at a heating rate of  $5\text{ K min}^{-1}$  in the temperature range from room temperature to 473 K. The temperature was kept for 1 h when reached at 473 K. Black and blue curves show the initial and the second temperature cycles, respectively.

### Conductivity and cyclic voltammetry measurements

The compacts of the products were prepared for the conductivity measurements by the two-probe ac technique. The synthesized powders were placed in an 8-mm-diameter die and then uniaxially pressed at 240–180 MPa. The resultant compacts were sandwiched by Li electrodes, and placed in a stainless steel electrochemical cell, as schematically illustrated elsewhere [S10]. The electrochemical cell was connected to a Chemical Impedance Meter (3532–80, Hioki Corp.). The input voltage perturbation and the frequency range were 100 mV and 1 M–4 Hz, respectively. The ac impedance measurements were carried out by temperature cycles from room temperature to 423 K with 10 K step intervals.

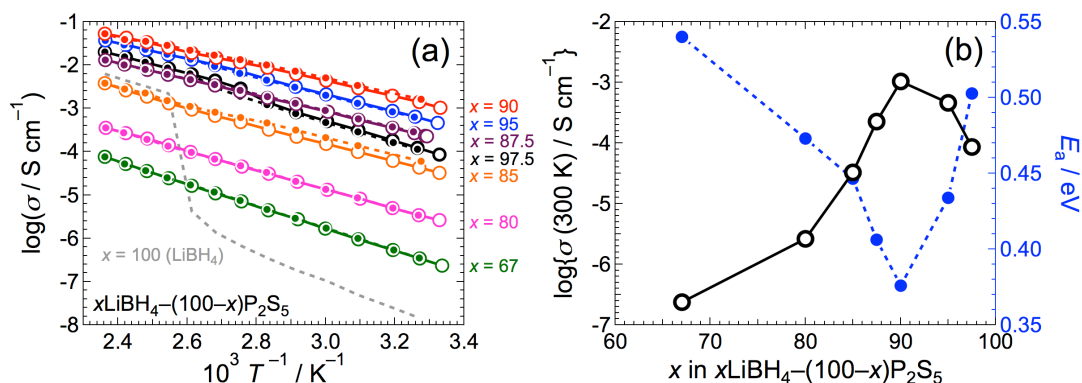
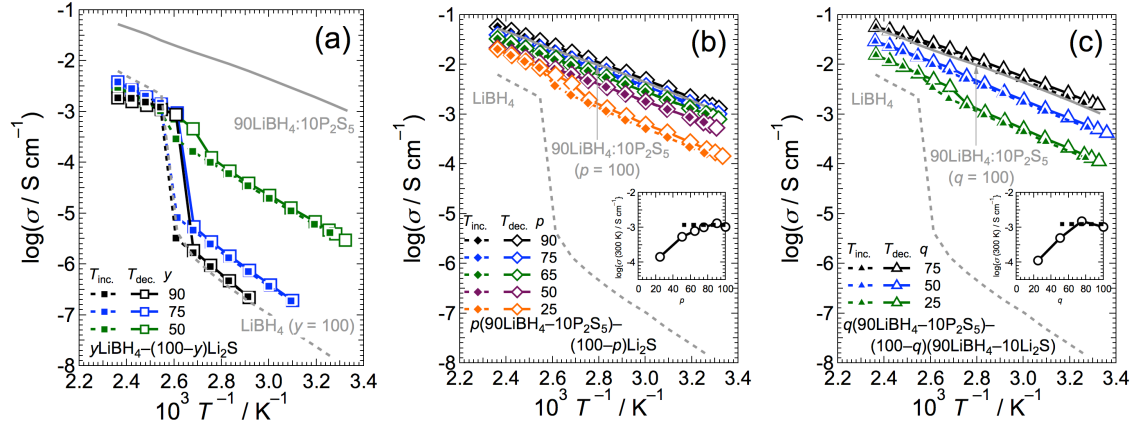


**FIGURE S5.** (a) Electrical conductivity of the pseudo-binary system,  $x\text{LiBH}_4-(100-x)\text{P}_2\text{S}_5$  ( $x = 100$  [S9], 97.5, 95, 90, 87.5, 85, 80 and 67), as a function of inverse temperature. (b) The ionic conductivity at 300 K, and the activation energies of  $x\text{LiBH}_4-(100-x)\text{P}_2\text{S}_5$  as a function of  $x$ . Closed and open symbols show the conductivities obtained during heating and cooling runs, respectively.

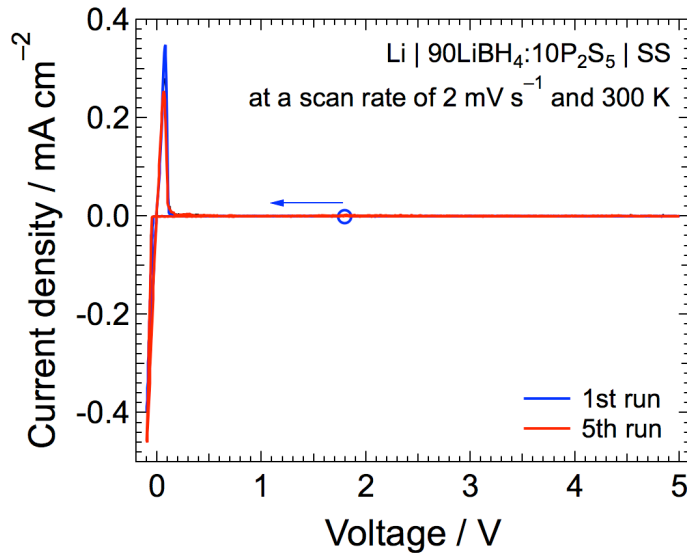
Figure S5 (a) shows electrical conductivities of  $x\text{LiBH}_4-(100-x)\text{P}_2\text{S}_5$  ( $x = 100$  [S9] and 97.5–67) as a function of inverse temperature. The electrical conductivities increased monotonically with increasing  $x$  for  $x \leq 90$ , while they decreased with increasing  $x$  for  $x \geq 90$ . The electrical conductivity at 300 K and the activation energies are shown in Fig. S5 (b). The electrical conductivity and the activation energy were the largest and the lowest for  $x = 90$ . These are  $\log\{\sigma(300 \text{ K}) / \text{S cm}^{-1}\} = -3.0$  and 0.38 eV, respectively. Considering the results together with the XRD measurements (Fig. S1 (a)), the fast lithium-ionic conducting crystalline phase precipitates in the highest concentration for  $x = 90$ . For  $x \geq 95$ , conductivity hysteresis is observed around the phase transition temperature of  $\text{LiBH}_4$ , i.e. 390 K [S9]. This suggests that remaining  $\text{LiBH}_4$  in  $x\text{LiBH}_4-(100-x)\text{P}_2\text{S}_5$  also contributed to the conductivity at temperatures higher than that temperature. This is consistent with the results of the XRD measurements.

Figure S6 (a), (b) and (c) show the electrical conductivities of pseudo-binary systems,  $y\text{LiBH}_4-(100-y)\text{Li}_2\text{S}$  ( $y = 90, 75$  and 50),  $p(90\text{LiBH}_4-10\text{P}_2\text{S}_5)-(100-p)\text{Li}_2\text{S}$  ( $p = 90, 75, 65, 50$  and 25) and  $q(90\text{LiBH}_4-10\text{P}_2\text{S}_5)-(100-q)(90\text{LiBH}_4-10\text{Li}_2\text{S})$  ( $q = 75, 50$  and 25), respectively. For  $y\text{LiBH}_4-(100-y)\text{Li}_2\text{S}$ , conductivity jumps around the phase transition temperature of  $\text{LiBH}_4$  were observed regardless of  $y$ . This means that any phase that possesses fast lithium-ionic conductivity is not included in this pseudo-binary system with a  $\text{LiBH}_4$ -rich region. For  $p(90\text{LiBH}_4-10\text{P}_2\text{S}_5)-(100-p)\text{Li}_2\text{S}$  and  $q(90\text{LiBH}_4-10\text{P}_2\text{S}_5)-(100-q)(90\text{LiBH}_4-10\text{Li}_2\text{S})$ , conductivities became close to that of  $90\text{LiBH}_4:10\text{P}_2\text{S}_5$  with increasing  $p$  and  $q$ . The fast lithium-ionic conduction phase is thus included only for  $90\text{LiBH}_4:10\text{P}_2\text{S}_5$ . Note that there were no clear indications of the existence of another crystalline phase except for  $\text{LiBH}_4$ ,  $\text{Li}_2\text{S}$  and  $90\text{LiBH}_4:10\text{P}_2\text{S}_5$  in the XRD patterns (data not shown). The results suggest that no other new crystalline phase is included in the system by means of our synthetic route employed in this study.

The results of XRD and conductivity measurements tell us that the concentration of the new crystalline phase becomes highest for  $x = 90$  in  $x\text{LiBH}_4-(100-x)\text{P}_2\text{S}_5$ , namely  $90\text{LiBH}_4:10\text{P}_2\text{S}_5$ , in the products. Thus, the  $90\text{LiBH}_4:10\text{P}_2\text{S}_5$  electrolyte was subjected to an electrochemical potential window analysis by a cyclic voltammetry (CV) measurement. The  $90\text{LiBH}_4:10\text{P}_2\text{S}_5$  electrolyte was sandwiched by Li and stainless-steel (SS) electrodes. The resultant asymmetric cell was connected to VersaSTAT4 (Princeton Applied Research). The measurement was carried out at 300 K and a  $2 \text{ mV s}^{-1}$  sweep rate in the voltage range from  $-0.1$  to 5 V. In the cyclic voltammogram, reversible lithium dissolution/stripping was observed nearly at 0 V, and no irreversible oxidation current appeared up to 5 V in the CV profiles. The results imply that the  $90\text{LiBH}_4:10\text{P}_2\text{S}_5$  electrolyte has a wide potential window, and thereby promises repeated operation of the bulk-type all-solid-state battery.



**FIGURE S6.** Electrical conductivities of pseudo-binary systems, (a)  $\gamma\text{LiBH}_4-(100-\gamma)\text{Li}_2\text{S}$  ( $\gamma = 90, 75$  and  $50$ ), (b)  $p(90\text{LiBH}_4-10\text{P}_2\text{S}_5)-(100-p)\text{Li}_2\text{S}$  ( $p = 90, 75, 65, 50$  and  $25$ ) and (c)  $q(90\text{LiBH}_4-10\text{P}_2\text{S}_5)-(100-q)(90\text{LiBH}_4-10\text{Li}_2\text{S})$  ( $q = 75, 50$  and  $25$ ) as a function of inverse temperature. The insets in (b) and (c) show the electrical conductivities at 300 K,  $\log\{\sigma(300\text{ K}) / \text{S cm}^{-1}\}$ , as functions of  $p$  and  $q$ , respectively. Closed and open symbols show the conductivities obtained during heating and cooling runs, respectively. Insets in (b) and (c):  $\log\{\sigma(300\text{ K}) / \text{S cm}^{-1}\}$  as functions of  $p$  and  $q$ , respectively.



**FIGURE S7.** Cyclic voltammogram of the asymmetric  $\text{Li} | 90\text{LiBH}_4:10\text{P}_2\text{S}_5 | \text{stainless-steel (SS)}$  cell operated at 300 K and a  $2\text{ mV s}^{-1}$  sweep rate with 5 cycles. The initial run started from an open blue circle toward low voltage.

### Battery test

$\text{TiS}_2$  (99.9 %, Sigma-Aldrich) and Li foil (Honjo Metal Co., Ltd.) were used as a positive electrode active material and negative electrode, respectively. The  $\text{TiS}_2$  and as-synthesized  $90\text{LiBH}_4:10\text{P}_2\text{S}_5$  powders were weighed in a 2:3 mass ratio, and mixed by an agate mortar in an agate pestle. The resultant powder was used for the composite positive electrode. We assembled here the bulk-type all-solid-state batteries with the following configurations:

- Battery-A;  $\text{TiS}_2/90\text{LiBH}_4:10\text{P}_2\text{S}_5 | 90\text{LiBH}_4:10\text{P}_2\text{S}_5 | \text{InLi}$  (discharge-charge profiles appearing in the main body of the manuscript, Fig. 3)
- Battery-B;  $\text{TiS}_2/90\text{LiBH}_4:10\text{P}_2\text{S}_5 | 90\text{LiBH}_4:10\text{P}_2\text{S}_5 | \text{Li}_4(\text{BH}_4)_3\text{I} | \text{Li}$

For the battery–A assembly, 6 mg of the composite positive electrode, 25 mg of the 90LiBH<sub>4</sub>:10P<sub>2</sub>S<sub>5</sub> electrolyte (500 μm thickness) were transferred in an 8-mm-diameter die, and uniaxially pressed at 240 MPa. The 10-mm-diameter In and Li foils (200 μm and 17 μm thicknesses, respectively) were placed in this order on the opposite of the positive electrode layer. The resultant battery was annealed at 343 K for 12 h for a negative electrode alloying, and subsequently temperature was decreased down to 300 K for the battery test. Prior to the battery–B assembly, Li<sub>4</sub>(BH<sub>4</sub>)<sub>3</sub>I was synthesized via the mechanical ball milling at 400 rpm for 5 h in Ar environment, and then used as an interlayer between the electrolyte and the lithium negative electrode. 6 mg of the composite positive electrode, 20 mg of the 90LiBH<sub>4</sub>:10P<sub>2</sub>S<sub>5</sub> and 5 mg of the Li<sub>4</sub>(BH<sub>4</sub>)<sub>3</sub>I were transferred in this order in an 8-mm-diameter die, and uniaxially pressed at 240 MPa (thickness was estimated to be approximately 100 μm for the composite positive electrode, 400 μm for the electrolyte and 70 μm for the interlayer). The Li foil was placed opposite of the positive electrode layer.

The assembled bulk-type all-solid-state TiS<sub>2</sub>/InLi and TiS<sub>2</sub>/Li batteries (the battery–A and –B, respectively) was transferred into a stainless steel electrochemical cell with a Teflon<sup>®</sup> guide. Microstructure and element distributions of the composite positive electrode were analyzed by a scanning electron microscope (SEM, JSM-6009, JEOL Ltd.) equipped with an energy dispersive X-ray spectrometer (EDS, EX-54175JMH, JEOL Ltd.). The assembled battery was connected to a 580 Battery Test System (Scribner Associates Inc.), and the battery tests were carried out with 0.1 C charge rate (114 μA cm<sup>-2</sup>) in the voltage range of 0.9–2.3 V for battery–A, and 0.05 C (57 μA cm<sup>-2</sup>) in 1.6–2.7 V for the battery–B at 300 K.

Highly deformable 90LiBH<sub>4</sub>:10P<sub>2</sub>S<sub>5</sub> new phase allows for inducing the extensive interfacial contact between TiS<sub>2</sub> and 90LiBH<sub>4</sub>:10P<sub>2</sub>S<sub>5</sub> phases in the composite positive electrode layer merely by a uniaxial pressing at 240 MPa and room temperature, as shown by the microstructure and element distributions in Fig. S8. Such a robust interface facilitates a smooth charge transfer reaction between the two phases, and thereby allowed a repeated operation of the bulk-type all-solid-state batteries at 300 K, as shown in Fig. 3 and Fig. S9.

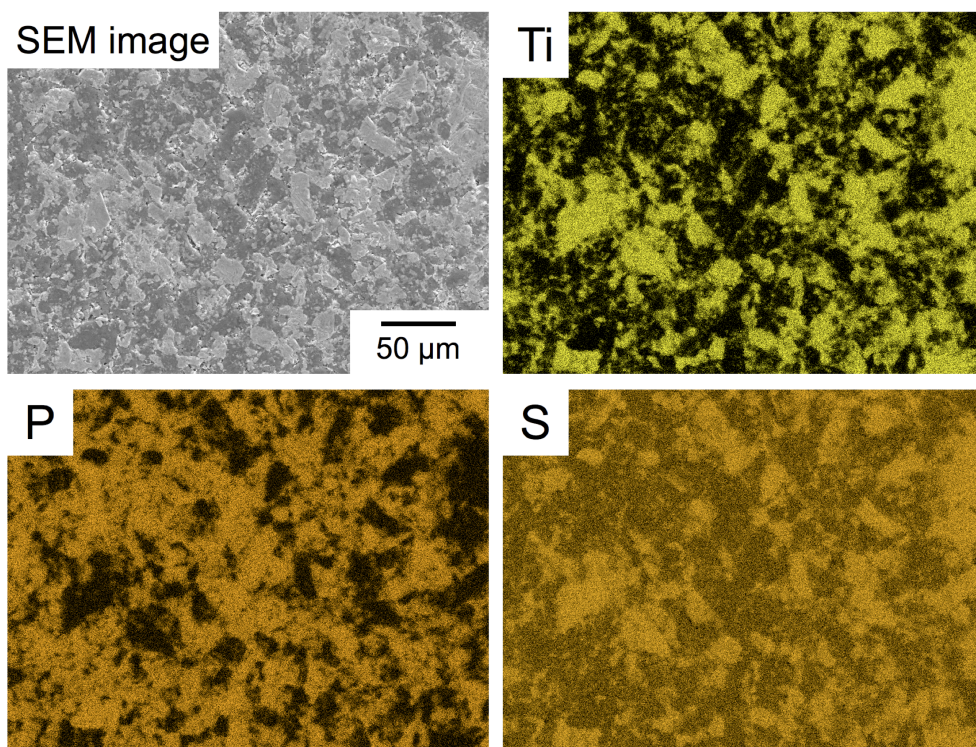


**FIGURE S8.** SEM image and distributions of Ti, P and S of the surface of the composite positive electrode consisting of TiS<sub>2</sub> and 90LiBH<sub>4</sub>:10P<sub>2</sub>S<sub>5</sub>.

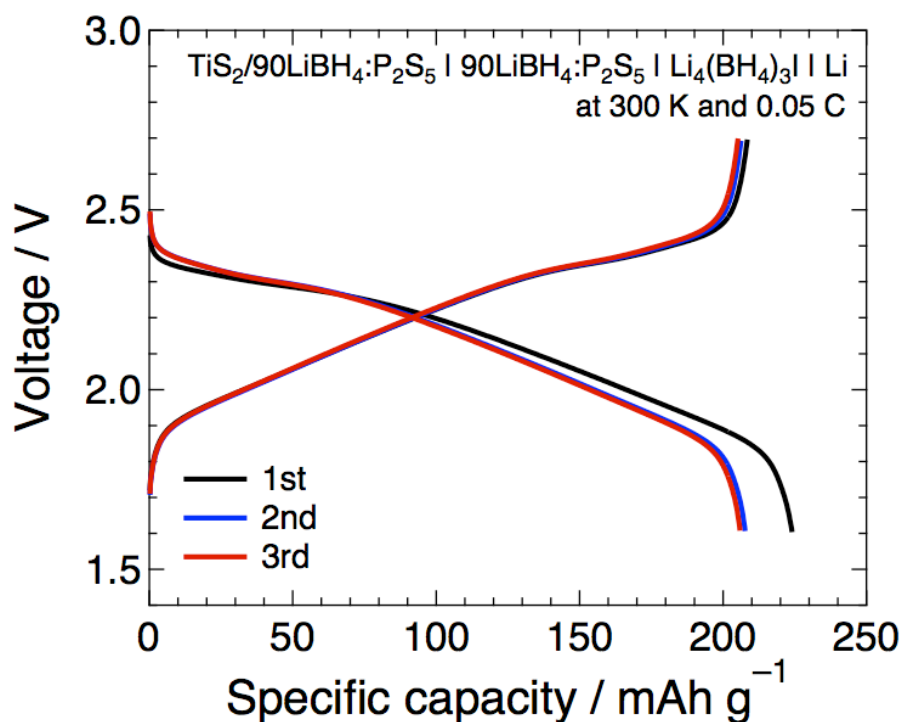


**FIGURE S9.** Discharge–charge profiles of the bulk-type all-solid-state  $\text{TiS}_2/\text{Li}$  battery (battery–B) using the  $90\text{LiBH}_4:10\text{P}_2\text{S}_5$  electrolyte operated at 300 K and 0.05 C ( $57 \mu\text{A cm}^{-2}$ ).

Figure S9 shows the 1<sup>st</sup>–3<sup>rd</sup> discharge–charge profiles of the bulk-type all-solid-state  $\text{TiS}_2/\text{Li}$  battery (battery–B) using the  $90\text{LiBH}_4:10\text{P}_2\text{S}_5$  electrolyte operated at 300 K and 0.05 C ( $57 \mu\text{A cm}^{-2}$ ). We placed the interlayer,  $\text{Li}_4(\text{BH}_4)_3\text{I}$ , for the inhibition of the reaction between the  $90\text{LiBH}_4:10\text{P}_2\text{S}_5$  electrolyte and Li negative electrode during charging. This issue is also overcome by employing the InLi alloy negative electrode as the discharge–charge profiles indicate in the main body of the manuscript, Fig. 3 (battery–A).  $\text{TiS}_2$  has a theoretical capacity of  $239 \text{mAh g}^{-1}$  [S11, S12]. Our battery exhibited the initial discharge and charge capacities of 224 and  $208 \text{mAh g}^{-1}$ , respectively, and coulombic efficiency was as high as 93 %. The reversible specific capacities of nearly  $205 \text{mAh g}^{-1}$  were achieved over the battery test.

## REFERENCES

- [S1] R. L. Paul, D. Sahin, J. C. Cook, C. Brocker, R. M. Lindstrom, D. J. O’Kelly, *J. Radioanal. Nucl. Chem.* 304 (2015) 189.  
[S2] T. J. Udovic, C. M. Brown, J. B. Leão, P. C. Brand, R. D. Jiggetts, R. Zeitoun, T. A. Pierce, I. Peral, J. R. D. Copley, Q. Huang, D. A. Neumann, R. J. Fields, *Nucl. Instr. And Meth. A* 588 (2008) 406.  
[S3] N. Verdal, T. J. Udovic, J. J. Rush, H. Wu, A. V. Skripov, *J. Phys. Chem. C* 117 (2013) 12010.  
[S4] S. Gadipelli, J. Ford, W. Zhou, H. Wu, T. J. Udovic, T. Yildirim, *Chem. Eur. J.* 17 (2011) 6043.  
[S5] Y. S. Chua, Q. Pei, X. Ju, W. Zhou, T. J. Udovic, G. Wu, Z. Xiong, P. Chen, H. Wu, *J. Phys. Chem. C* 118 (2014) 11344.  
[S6] A. Meyer, R. M. Dimeo, P. M. Gehring, D. A. Neumann, *Rev. Sci. Instrum.* 74 (2003) 2759.  
[S7] J. R. D. Copley, J. C. Cook, *Chem. Phys.* 292 (2003) 477.  
[S8] R. T. Azuah, L. R. Kneller, Y. Qiu, P. L. W. Tregenna-Piggott, C. M. Brown, J. R. D. Copley, R. M. Dimeo, *J. Res. Natl. Inst. Stan.* 114 (2009) 341.  
[S9] M. Matsuo, Y. Nakamori, S. Orimo, H. Maekawa, H. Takamura, *Appl. Phys. Lett.* 91 (2007) 224103.  
[S10] A. Unemoto, S. Yasaku, G. Nogami, M. Tazawa, M. Taniguchi, M. Matsuo, T. Ikeshoji, S. Orimo, *Appl. Phys. Lett.* 105 (2014) 083901.  
[S11] M. S. Whittingham, *Science* 192 (1976) 1126.  
[S12] M. S. Whittingham, *Prog. Solid State Chem.* 12 (1978) 41.